RSC Advances

PAPER

View Article Online
View Journal | View Issue

Cite this: *RSC Adv.*, 2020, **10**, 36654

Investigation on the composition and corrosion resistance of cerium-based conversion treatment by alkaline methods on aluminum alloy 6063

Cen Lu,[a] Songlin Mu,*[a] Jun Du,[a] Kai Zhang,[b] Mincheng Guo[a] and Ling Chen[a]

Cerium conversion coating (CeCC) and Ce–Mo conversion coating (CeMCC) were prepared on aluminum alloy 6063 (AA6063) by immersion in alkaline conversion baths. Surface morphology and composition of the conversion coatings were characterized by scanning electron microscopy (SEM) and X-ray photoelectron spectroscopy (XPS). And electrochemical measurements were used to assess corrosion performance of the coatings. The SEM observations showed that CeMCC possessed a smoother and more uniform structure than CeCC, and the thickness of CeCC and CeMCC was about 0.8 and 1.2 μm respectively. The XPS depth analysis indicated that CeMCC contained a considerable amount of molybdenum and the cerium content was higher than that of CeCC at all coating depths. CeCC comprised of Al_2O_3, Ce_2O_3, CeO_2, and cerium hydroxides, and the composition of CeMCC also included MoO_2, MoO_3, $Al_2(MoO_4)_3$ and Na_2MoO_4 besides the above mentioned components. A potentiodynamic polarization (PDP) test revealed that the corrosion current density (i_{corr}) values for bare alloy and CeCC were 13.36 and 4.38 μA cm^{-2} respectively in 3.5 wt% NaCl solution, while CeMCC exhibited the lowest i_{corr} value of 0.24 μA cm^{-2}, about two orders of magnitude lower than that of the substrate. Furthermore, the results obtained from both a cupric sulfate drop test and electrochemical impedance spectroscopy (EIS) characterization suggested that CeMCC possessed higher corrosion resistance in comparison with CeCC.

Received 21st August 2020
Accepted 26th September 2020

DOI: 10.1039/d0ra07201j

rsc.li/rsc-advances

Introduction

Aluminum alloys are widely used in aerospace, shipping, architecture, and 3C electronic products because of their high strength/weight ratio, excellent electrical and thermal conductivity, and good machining performance.[1–3] However, the high chemical activity of aluminum makes it particularly liable to corrosion. In a slightly harsh (such as humid) environment, especially in the presence of Cl^-, aluminum and its alloys are prone to localized corrosion, including pitting corrosion, crevice corrosion, intergranular corrosion and stress corrosion cracking, which seriously shortens the service life of aluminum products.[4] Hence, there is an urgent need to improve the corrosion resistance of aluminum alloys prior to its application. Chemical conversion treatment is known as a very important approach to achieve appropriate corrosion resistance for metals surface due to its simple processing equipment, easy operation, and low cost.[5] While as the most common traditional anticorrosive treatment, chromate conversion treatment with remarkable corrosion performance and favorable adhesion, has been used in industrial applications for several decades.[6] However, European Union has banned the use of hexavalent chromium through RoHS and WEEE regulations because of its highly toxic and carcinogenic nature, which brings about many serious environmental and health-related problems.[7] Therefore, considerable effort has been devoted to developing viable alternatives to chromate, including permanganate,[8] phosphate,[9] titanate/zirconate,[10] molybdate,[7] and rare earth salts.[11–15]

Extensive researches have shown that rare earth metal (REM) salts are effective inhibitors for corrosion protection of aluminum alloys,[12,15–17] zinc,[18] magnesium,[11,14,19] steel,[20] and metal matrix composites.[13,21,22] Due to the non-toxicity and acceptable anticorrosive property of REM salts,[23] rare earth conversion treatment of aluminum alloys is considered to be one of the most promising substitutes for chromate conversion treatment.[11,15,17,19] In addition, most studies imply that cerium salts show better corrosion protection than other REM salts.[24,25] K. A. Yasakau *et al.*[26,27] synthesized amorphous cerium molybdate nanowires, which was used alone or as corrosion inhibitor in sol–gel coatings for protection of 2024 aluminum alloy, and the mechanism of active protection was based on the high solubility of cerium molybdate nanomaterials. Various addition of inorganic and/or organic additives have been used to modify the microstructure and

[a]*School of Materials Science and Engineering, South China University of Technology, Wu Shan Road 381, Tian He District, Guangzhou 510640, China. E-mail: mslucen95@mail.scut.edu.cn; musonglin@scut.edu.cn; Fax: +86 20 8711 3747; Tel: +86 20 8711 3747*

[b]*GuangDong Provincial Academy of Building Research Group Co.,Ltd, Guangzhou 510500, China*

corrosion resistance of cerium-based conversion coatings. Z. Mahidashti *et al.*[28] studied the effect of CeCC modified by lanthanum as additive and post-treatment on the corrosion resistance and surface morphology of the mild steel. They found that the CeCC with 0.4 g L^{-1} La additive or post-treated by the same amount of La for 90 s exhibit the best anti-corrosion performance compared to the CeCC and untreated steel. Mohamed *et al.*[29] examined the synergistic inhibition effect of Ce^{4+} and melamine on the corrosion of aluminum alloy 2024 (AA2024) in 3.5% NaCl solution. Results of this study showed that a combination of 50% Ce^{4+} and 50% melamine results in the lowest corrosion rates, and the mechanism of protection revealed that the reduction of Ce^{4+} to Ce^{3+} occurs during corrosion protection of AA2024. In another study, the synergistic effect of cerium acetate and sodium sulfate on corrosion inhibition of AA2024-T3 was studied by Peter *et al.*[30] The results present a more effective corrosion inhibition of AA2024-T3 immersed in NaCl + $Ce(OAc)_3$ solution with Na_2SO_4 owing to a synergistic effect leading to the formation of more compact and more durable film. Furthermore, the authors also investigated the synergistic or adverse effects of additives NaOAc, $NaNO_3$ and Na_2SO_4 on the performance of $Ce(OAc)_3$ as inhibitor of corrosion of aluminum alloy 7075-T6 in 0.1 M NaCl solution, and the most efficient corrosion inhibition was attained by synergism between $Ce(OAc)_3$ and Na_2SO_4 and attributed to low solubility of the product formed.[31] Maryam *et al.*[32] have utilized H_2O_2 and NaCl to accelerate the formation of CeCC deposited on high pressure die cast (HPDC) Al–Si alloys. The results showed that NaCl promotes micro-galvanic coupling accelerating the corrosion reactions and thus the coating deposition, and H_2O_2 accelerates cerium hydroxide/oxide precipitation and modifies the coating morphology from localized deposited islands to a continuous layer with a crack-mud structure in some regions. Kanani *et al.*[33] developed a cerium-based conversion treatment on aluminum 6063 with the addition of glycerin and H_2O_2. They found that immersion time in the conversion solution had an important influence on the corrosion performance and the optimum coating behavior was achieved by 600 s immersion. Hossein *et al.*[34] studied the effect of chitosan on cracking and corrosion behavior of cerium oxide conversion coating on AA2024. The result showed that the cracking of coating was reduced noticeably by adding chitosan to the solution and the coating exhibited extremely high corrosion resistance when the content of chitosan was 0.01 wt%.

In order to improve the coating formation rate, oxidants (H_2O_2,[22,35,36] $KMnO_4$,[37] *etc.*) and accelerators (for instance NaCl[38] and NaF[10]) are often added to the rare earth conversion solution. It is worth noting that most researches were conducted in acidic conversion baths, which exhibited poor stability. As is known to all, H_2O_2 is easy to decompose in aqueous solution, accelerating the aging of conversion solution; $KMnO_4$ itself is not stable enough, and it is apt to be reduced to low valence oxides (such as MnO_2 precipitation) in solution containing accelerators and Ce^{3+}, while in turn MnO_2 will accelerate the decomposition of $KMnO_4$ and make it lose its oxidation property.[39] All of this leads to poor stability of acidic baths, fast aging of conversion solution and short service life. However, the use of liquid acid can be avoided in alkaline conversion solution, making the operation safer. In addition, there is no acid mist in the alkaline one, which will not cause damage to workers' health. In contrast with the abundant studies of acidic treatment, the research on alkaline conversion treatment, especially on the rare earth involved alkaline treatment, is considerably rare. In this paper, $Ce(NO_3)_3$ was used as the main salts of the conversion bath, EDTA-2Na was used as the complexing agent, and the rare earth conversion treatment was conducted under alkaline condition. Moreover, Na_2MoO_4 was added into the alkaline bath for comparison. The microstructure, composition and corrosion resistance of the coatings were investigated by means of scanning electron microscopy (SEM), energy dispersive X-ray spectroscopy (EDS), X-ray photoelectron spectroscopy (XPS), and electrochemical workstation, respectively.

Experimental

Materials and treatment process

The material used in this study was AA6063 aluminum alloy panels, bought from Dongguan GuanMei Metal Materials Co., Ltd, of size 30 mm × 30 mm × 3 mm, with the chemical composition (in wt%) of 0.95 Mg, 0.43 Si, 0.22 Cu, 0.10 Zn, 0.22 Cr, 0.20 Fe, 0.01 Mn, 0.02 Ti, and Al balance.

The specimens were successively wet ground to 1000 grade by SiC abrasive papers. Then, the specimens were ultrasonically cleaned in ethanol for 5 min and rinsed in deionized water. In order to fully remove the native oxide layer from the surface of aluminum alloy, a chemical pretreatment was conducted by the following method: etched in industrial acid (containing H_2SO_4, H_3PO_4, HF, and emulsifier OP-10) at room temperature for 1 min, rinsed three times with deionized water, then etched in mixed acid solution which contained HNO_3, H_3PO_4 and H_2SO_4 at room temperature for 2 min, rinsed three times with deionized water. The acid etching promoted the activation of the specimen surface favoring the formation of conversion coating on the substrate. When the pretreatment was finished, conversion treatment was carried out immediately to avoid the surface of the samples to be oxidized again. After the preliminary exploration experiments, the components of alkaline conversion bath were optimized as follows: urea 20 g L^{-1}, $Ce(NO_3)_3 \cdot 6H_2O$ 8 g L^{-1}, EDTA-2Na 4 g L^{-1}, Na_2CO_3 5 g L^{-1}. The pH value of the solution was adjusted around 9 by 50 g L^{-1} Na_2CO_3 solution. Samples were prepared by immersion of the aluminum alloy panels in bath at 70 °C for 20 min. To study the effect of molybdate on the CeCC, 10 g L^{-1} $Na_2MoO_4 \cdot 2H_2O$ was added to obtain CeMCC, and the conversion treatment was performed under the same conditions (temperature and treatment time) as aforementioned. Conversion treated samples were then dried and aged in ambient condition for about 24 h before further microstructural characterization and electrochemical measurements. All the reagents used were AR grade, bought from Guangzhou Chemical Reagent Factory.

Surface characterization

The surface morphology and microstructure of the conversion coatings were characterized by field emission scanning electron

microscopy (FESEM, Merlin, Zeiss, Germany), under high vacuum condition with 5 kV beam energy. An EDS system attached to FESEM was employed to examine the chemical composition of the conversion coatings.

The chemical state of elements presented in the conversion coatings were investigated by X-ray photoelectron spectroscopy (XPS, Thermo K-Alpha$^+$). A monochromatic Al Kα (1486.8 eV) X-ray source (analysis area was *c.a.* 400 μm^2) was used in the XPS, which was operated at 15 kV and 10 mA, along with pressure in the analysis chamber of 2×10^{-9} mbar. Overview spectra were recorded in the energy range of 1350 to 0 eV with pass energy of 150 eV. The elemental composition depth profiles of the coatings were analyzed by way of Ar^+ sputtering. Firstly, the XPS data were collected on the outermost surface of the samples, then the surface was sputtered by Ar^+ for 5 min, the XPS data were collected again. This sputtering-collection process was repeated for 9 times on each conversion coating. While as for the high-resolution spectra, the pass energy and energy step of the analyzer were 30 eV and 0.05 eV respectively. The binding energy (BE) of obtained data was calibrated by a linear shift so that the peak of the C 1s originated from adventitious carbon corresponded to 284.8 eV.[40] The experimental data were curve fitted by XPSPEAK 4.1 software after background subtraction. The background shape was Shirley, and Lorentzian–Gaussion

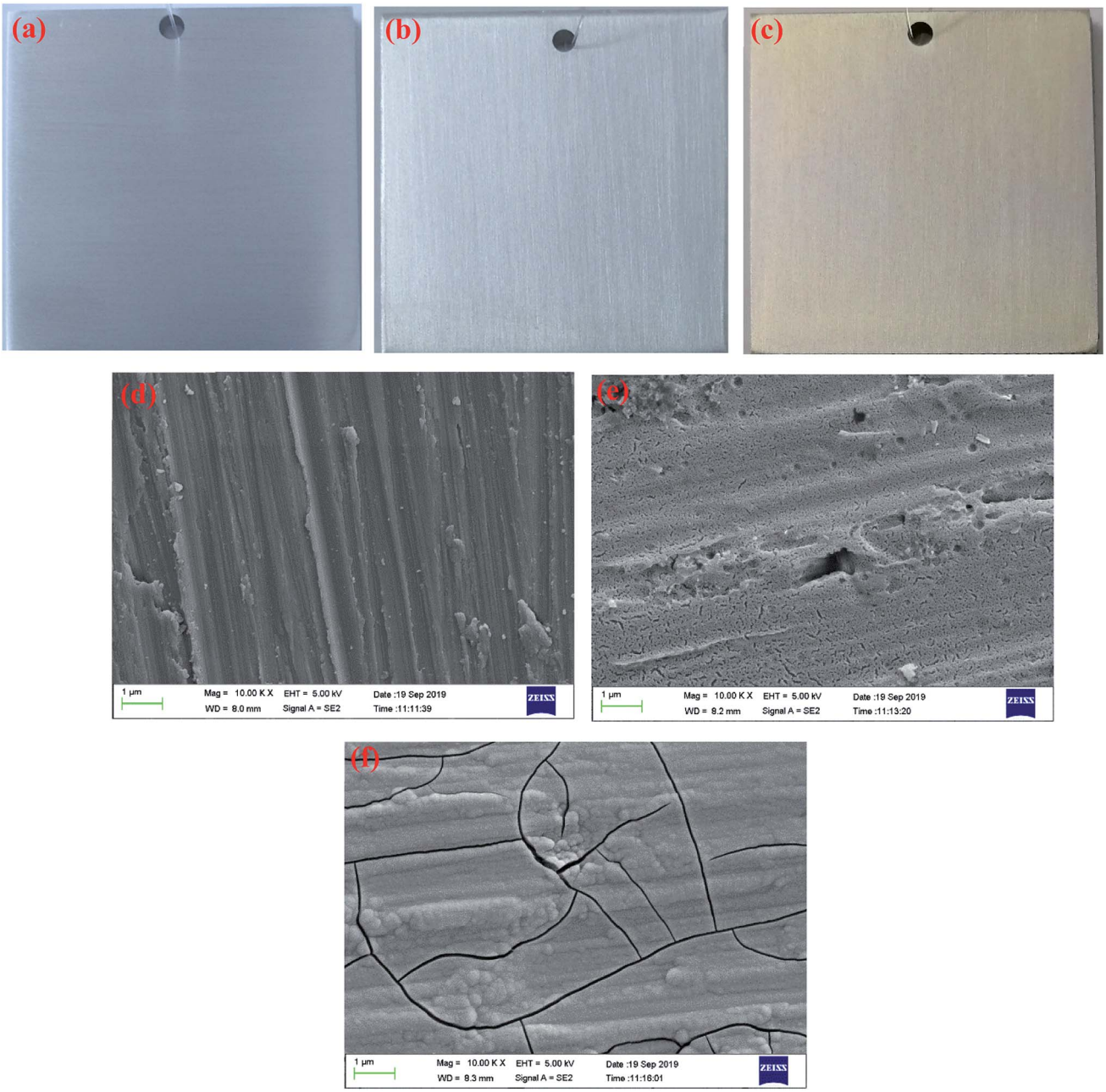

Fig. 1 Digital photos and SEM images of bare AA6063 (a and d), CeCC (b and e) and CeMCC (c and f).

Table 1 The elemental contents of the spots marked in Fig. 2

Spots		Elemental contents Al	O	Ce	Mo	Mg	Si	Cr	Fe
1	wt%	87.88	7.24	3.55	—	0.84	0.49	—	—
	at.%	86.37	11.62	0.67	—	0.89	0.45	—	—
2	wt%	58.41	12.66	5.41	—	0.45	5.34	2.35	15.38
	at.%	61.43	22.45	1.10	—	0.53	5.40	1.28	7.81
3	wt%	74.83	13.37	2.19	8.59	0.59	0.43	—	—
	at.%	73.88	22.26	0.42	2.38	0.65	0.41	—	—
4	wt%	72.65	12.37	3.57	11.40	—	—	—	—
	at.%	74.58	21.42	0.71	3.29	—	—	—	—

ratio was fixed at 20%. The $\sum\chi^2$ (the degree of deviation between actual value and theoretical value) values of fitted results were less than 10.

Cupric sulfate drop experiment and electrochemical measurements

The cupric sulfate drop test was carried out to quickly evaluate the corrosion resistance of the samples, with solution composed of 2 g $CuSO_4 \cdot 5H_2O$, 2 mL hydrochloric acid and 98 mL deionized water. When the solution was dropped on the surface – start time; when the color of the dropped region changed from blue to dark red – end time. To guarantee the reliability of the data, four points were taken on the surface of each sample, and the mean time was taken as the anticorrosion time of the sample. The recorded time was used to evaluate the corrosion performance of the coatings.

Electrochemical measurements including EIS and PDP were performed in 3.5 wt% NaCl solution at room temperature with a CHI604E electrochemical workstation. A conventional three-electrode cell was employed for electrochemical tests, where the working electrode was the samples with an exposure area of 1.0 cm^2, the reference electrode was a saturated calomel electrode (SCE), and the counter electrode was a platinum sheet of 1.5 cm^2. The ratio of corrosive solution to tested area is 250 mL to 1 cm^2. The working electrode was immersed in testing electrolyte for 10 min to establish a steady open circuit potential (E_{ocp}) before EIS experiment. The EIS measurements were conducted in the frequency range from 100 kHz to 10 mHz and the sinusoidal amplitude of 10 mV with respect to the E_{ocp}. After the EIS tests, the PDP measurements were carried out at the same position of the samples. The purpose to do this is to avoid the error caused by different testing locations. The potential was scanned from −300 to +300 mV *versus* E_{ocp} at a scanning rate of 2 mV s^{-1}. And three different spots on the samples were tested to confirm the reproducibility of the electrochemical measurements.

Results and discussion

SEM studies

The digital photos of the samples before and after conversion treatment are displayed in Fig. 1. As shown in Fig. 1(b) and (c), the prepared CeCC is colorless and transparent, and the CeMCC exhibits a uniform brown appearance. Fig. 1(d)–(f) depict the microstructure of AA6063, CeCC and CeMCC under SEM observation. The scratches and abrasive dust originated from the abrading procedure are still clearly visible for the bare AA6063. From the Fig. 1(e), there are a few corrosion pits and a great many of small strip-shaped crevices on the surface of CeCC, which is mainly due to random dissolution of intermetallic particles (IMPs) during the acid etching step,[35] and the layer is relatively loose. As is evident in Fig. 1(f), a smooth, continuous and uniform "dried-riverbed"-shaped coating with some bulge of spherical particles has completely covered the entire surface of aluminum alloy. However, the CeMCC surface also shows some micro-cracks, which were mainly created by internal stress release resulted from the coating shrinkage during the drying process.[21] From the SEM images the CeMCC possesses more compact structure compared with the CeCC.

Table 1 exhibits the elemental contents of the four spots marked in Fig. 2. The EDS measurement shows the presence of Ce (3.55 wt%), Al (87.88 wt%) and O (7.24 wt%) on spot 1 for CeCC. It can be expected that the CeCC may be composed of oxides and/or hydroxides of aluminum and cerium. As shown in Fig. 2(a), there are some irregular white regions in the CeCC. According to the corresponding EDS spectrum on spot 2, in which Ce, Al and O account for 5.41 wt%, 58.41 wt% and 12.66 wt% respectively. And the content of Si, Fe and Cr in this

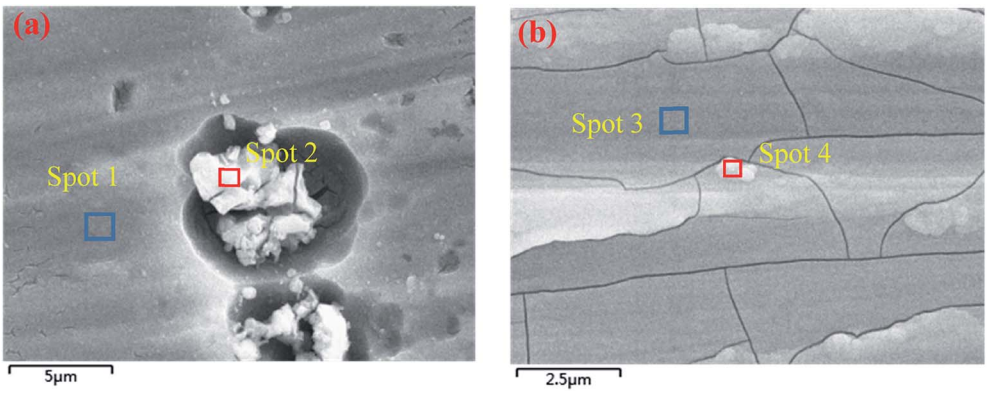

Fig. 2 EDS illustrations for CeCC (a) and CeMCC (b).

area is significantly increased in comparison with the matrix composition due to the presence of Al(Fe, Cr)Si intermetallic compounds. The amount of Ce on the intermetallic compounds is higher than that on areas without intermetallics, indicating that the deposition of Ce occurred preferentially at the location of Fe-rich intermetallics thanks to their cathodic behavior with respect to the aluminum matrix.[41] In the case of CeMCC (Fig. 2(b)), elements such as Al (74.83 wt%), Ce (2.19 wt%), Mo (8.59 wt%) and O (13.37 wt%) have been detected on its surface (spot 3), which may consist of oxides and/or hydroxides of aluminum, cerium and molybdenum. A white particle (spot 4) can be seen in the CeMCC, mainly containing elements of Al (72.65 wt%), Ce (3.57 wt%), Mo (11.40 wt%), and O (12.37 wt%). Obviously, the amount of Ce and Mo on spot 4 is higher than that on spot 3, while the content of Al and O is just the opposite. It is worthy to note that the amount of Ce is decreased in the CeMCC (2.19 wt% Ce) compared to the CeCC (3.55 wt% Ce), this decrease may be resulted from the co-deposition of Mo compounds, because the anions of Mo compounds should combine with Ce ions to form Ce insoluble compounds if there is no Mo ions. Besides, the Al content (74.83 wt%) in the CeMCC is lower than that (87.88 wt%) of CeCC, while the O (13.37 wt%) content in the CeMCC is nearly twice as much as that (7.24 wt%) of CeCC. The EDS results show that both CeCC and CeMCC may be composed of oxides, hydroxides of the inorganic elements (Al, Ce, Mo).

Fig. 3 shows the cross-sectional SEM images and line-scanning EDS spectra of CeCC and CeMCC. In order to highlight the elements of cerium and molybdenum, aluminum with strong signal is not added in the EDS spectra. It can be observed from Fig. 3(a and b) that the O content of the CeCC increases evidently along with scanning line, while the Ce content presents a slight increase. The cross-sectional micrograph and line-scanning spectrum of CeCC exhibit that the thickness of the coating is about 0.8 μm. As shown in Fig. 3(c and d), the content of O and Mo in the CeMCC is obviously higher than that in the matrix, and the Ce content shows a slight increase. Thus it can be deduced that the main components of the CeMCC are oxides of Al, Mo and Ce. And according to the peak of element Mo, the coating thickness of the CeMCC is 1.2 μm or so.

XPS investigation

XPS was utilized to further analyze the element composition and chemical valence of the conversion coatings. Fig. 4 presents

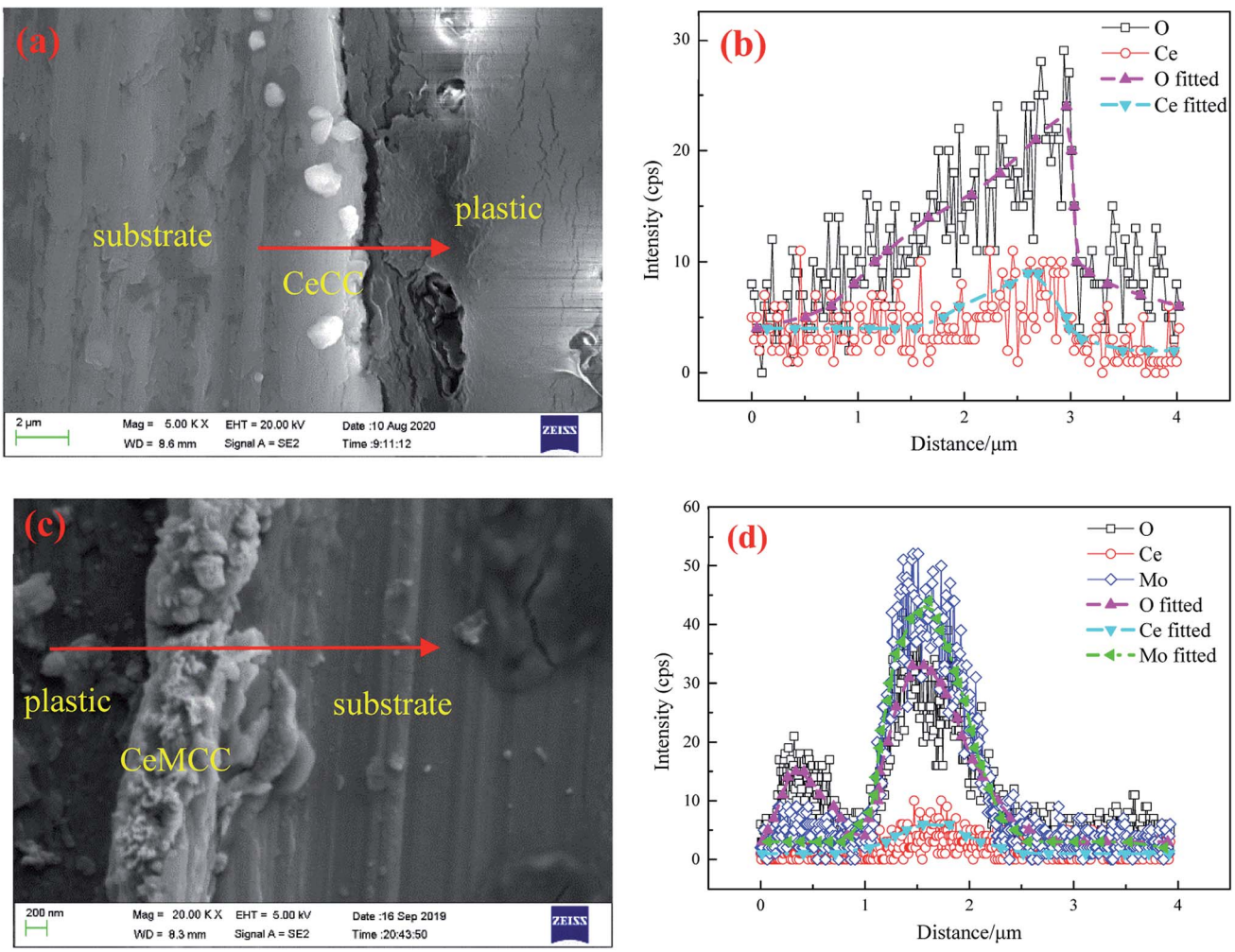

Fig. 3 Cross-sectional images and line-scanning EDS spectra of CeCC (a and b) and CeMCC (c and d).

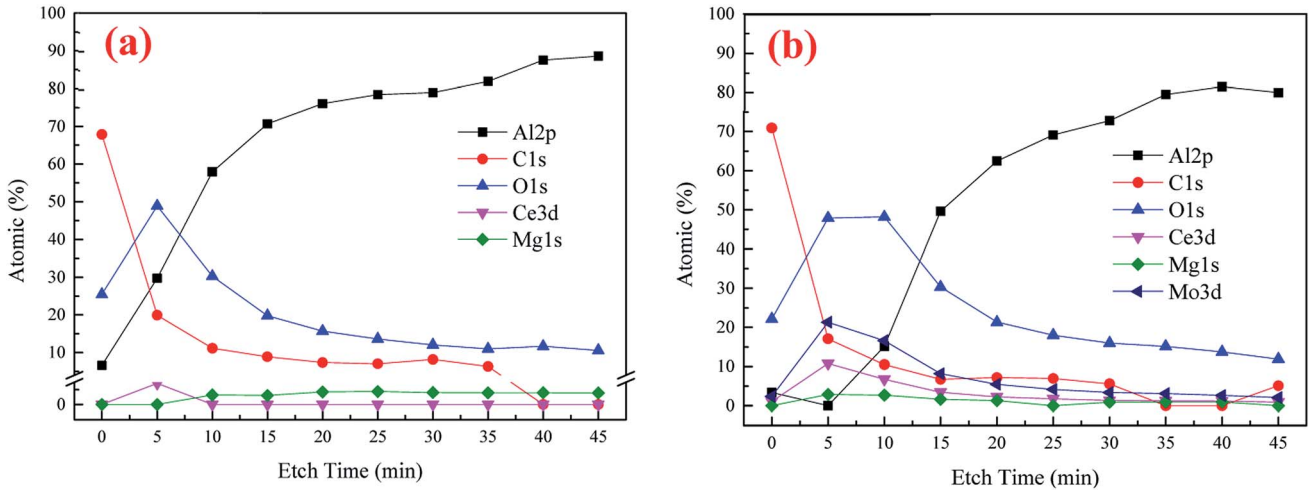

Fig. 4 The XPS depth profile spectra of conversion coatings: (a) CeCC, (b) CeMCC.

the depth profile spectra for CeCC and CeMCC. Both the CeCC and CeMCC were sputtered 9 layers and each layer was sputtered for 5 min. As can be seen in Fig. 4(a), as the Ar^+ etch time increases from 0 to 15 min, the Al content increases sharply from 6.6 at% to 70.6 at%, while the C content decreases from 67.9 at% to 8.9 at%. Then the amount of Al slowly increases and C slowly decreases as a function of the etch time. A considerable amount of O is detected in the CeCC. After sputtering for 5 min,

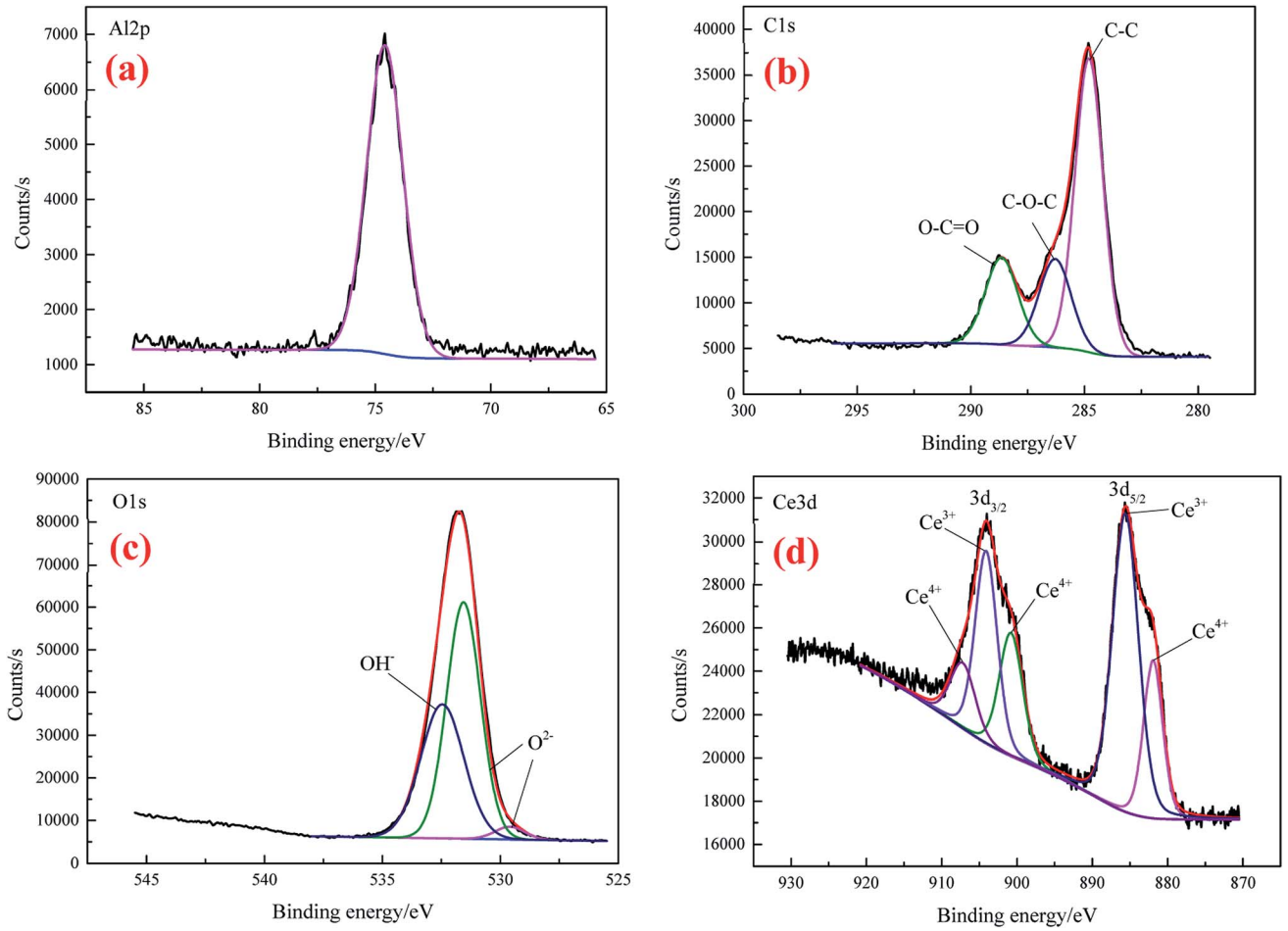

Fig. 5 The high-resolution XPS spectra of Al 2p (a), C 1s (b), O 1s (c), and Ce 3d (d) for CeCC.

the maximum value of O element reaches about 50 at% and then it decreases slowly. The amount of O decreases to its initial value after about 12 min of sputtering. As for the element Ce, the low concentration (1.4 at%) indicates that the deposited cerium oxides only covered a small fraction of the whole surface area, mainly located at the Al(Fe, Cr)Si intermetallics.[42] Similar to the CeCC, the C curve of CeMCC varies significantly after 5 min of sputtering because of the removal of surface carbon. The content of C decreases sharply from 70.9 at% in the outermost surface to 17.1 at% in the 5 min-sputtering layer. It is worth noting that after 5 min of sputtering the contents of Ce, Mo and O reach their maximum, 10.8 at%, 21.3 at% and 47.9 at% respectively. It suggests that the outer layer of CeMCC may be mainly composed of oxides and/or hydroxides of Ce and Mo.

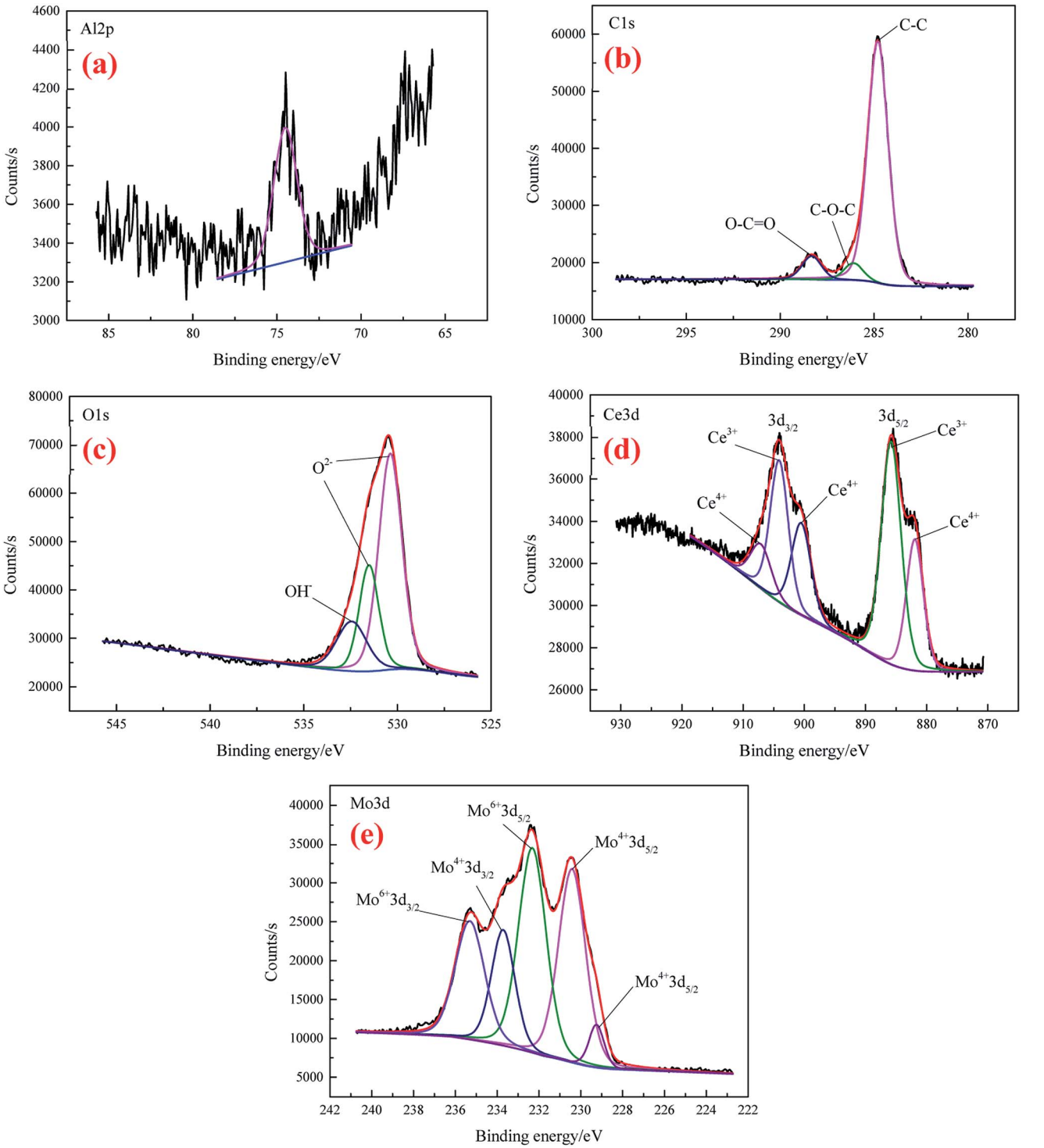

Fig. 6 The high-resolution XPS spectra of Al 2p (a), C 1s (b), O 1s (c), Ce 3d (d), and Mo 3d (e) for CeMCC.

In addition, the O curve exhibits an elongated peak between 5 and 10 min of sputtering, while the O curve for CeCC appears a peak at 5 min-sputtering position. This may imply that the coating thickness of CeMCC is larger than that of CeCC, which is in accordance with the result of line-scanning (Fig. 3). After 20 min of sputtering, the contents of O, C, Mo and Ce gradually decrease with the sputtering time, while the Al curve shows the opposite behavior. By the XPS analysis of the element content with the coating depth, it can be concluded that the content of Ce in the CeMCC is higher than that in the CeCC at all coating depths, which indicates that the addition of molybdate may promote the deposition of cerium insoluble compound(s).

The high-resolution spectra of Al 2p, C 1s, O 1s and Ce 3d for CeCC are presented in Fig. 5. The peak of Al 2p observed at BE of 74.58 eV suggests the presence of Al_2O_3.[43]

The C 1s (Fig. 5(b)) can be fitted with three peaks at 284.8 eV, 286.29 eV and 288.65 eV, which are assigned to the peak of C–C, the amorphous carbon C–O–C on the natural aluminum oxide and the carboxyl carbon O–C=O (derived from EDTA-2Na), respectively.[40,44] As shown in the XPS spectrum of O 1s (Fig. 5(c)), the peak with BE of 529.6 eV is consistent with the characteristic peak of CeO_2,[45] the O^{2-} component located at 531.46 eV is attributed to the coexistence of Ce_2O_3 (BE O 1s = 530.2 eV) and Al_2O_3 (BE O 1s = 531.9 eV),[36] while the peak centered at 532.46 eV matches closely to the BE of Ce–OH group.[44] Thus the element O in the CeCC may come from Al_2O_3, CeO_2, Ce_2O_3, and cerium hydroxides. It is reasonable that the presence of partial C and O may be due to the accumulation of contaminants during exposure to air. The physical and chemical perturbation of the surface influenced the Ce 3d electron emission which displays a noisy signal.[17] From the Fig. 5(d), it is evident that Ce 3d exhibits a broad and complex spectrum which reveals the presence of multiple oxidation states for Ce. The Ce 3d spectrum is fitted in spin–orbit doublets of Ce $3d_{5/2}$ and Ce $3d_{3/2}$. The peaks at 881.93 eV and 900.8 eV are corresponding to the satellite peaks of Ce^{4+} $3d_{5/2}$ and Ce^{4+} $3d_{3/2}$ respectively, which should be originated from Ce–O bonding in CeO_2.[46–48] The signals of Ce^{3+} $3d_{5/2}$ and Ce^{3+} $3d_{3/2}$ spin–orbit doublets are observed at BE of 885.6 eV and 904.1 eV, respectively, which can be assigned to Ce_2O_3.[46] While the shoulder at 907.2 eV of Ce^{4+} $3d_{3/2}$ can be attributed to the presence of CeO_2.[46] Accordingly, both the O 1s and Ce 3d spectra indicate that cerium in the CeCC existed in trivalent and tetravalent states, and the peak area of Ce(III) is about 59% higher than that of Ce(IV). It can be inferred that a considerable part of Ce^{3+} was oxidized to Ce^{4+} during the conversion process ($O_2 + 2H_2O + 2e \rightarrow H_2O_2 + 2OH^-$, $Ce^{3+} + H_2O_2 + 2OH^- \rightarrow Ce(OH)_4$ ($CeO_2 \cdot 2H_2O$)↓),[49] since the main salt of conversion bath was cerium(III) nitrate. The results above reveal that CeCC is comprised of Al_2O_3, Ce_2O_3, CeO_2, and cerium hydroxides.

The high-resolution spectra of Al 2p, C 1s, O 1s, Ce 3d, and Mo 3d for CeMCC are shown in Fig. 6(a)–(e), respectively. It can be seen that the noise in Al 2p spectrum (Fig. 6(a)) is extensive, and the intensity is lower than that of CeCC, implying less proportion of aluminum in the coating. The Al 2p peak that appeared at 74.5 eV is possibly attributed to the compounds Al_2O_3 and $Al_2(MoO_4)_3$.[43,50] The C 1s spectrum (Fig. 6(b)) clearly exhibits that peak components centered at BE of 284.8 eV, 286.1 eV and 288.32 eV are ascribed to C–C bonding, C–O bonding and the carboxyl carbon O–C=O group (originated from EDTA-2Na) respectively.[40,44] As can be seen in Fig. 6(c), the O 1s core-level spectrum was curve-fitted into three peak components. The peak observed at 530.38 eV can be ascribed to the oxygen in Ce_2O_3, MoO_2 or/and $Al_2(MoO_4)_3$,[36,51,52] while the peaks at BE of 531.52 eV and 532.44 eV are respectively assigned to the presence of Al_2O_3 or/and MoO_3, and cerium hydroxides.[44,53] The BE of 885.8 eV and 904.1 eV in Ce 3d spectrum (Fig. 6(d)) respectively represent the Ce $3d_{5/2}$ and Ce $3d_{3/2}$ of Ce_2O_3,[46] while the peaks for CeO_2 are observed at 881.93 eV, 900.5 eV, and 907.1 eV, associating with Ce $3d_{5/2}$ and Ce $3d_{3/2}$ photoelectron line of cerium.[46,48] The area ratio of Ce(III) to Ce(IV) is about 1.42, which is lower than that of CeCC, indicating more Ce^{3+} are oxidized to Ce^{4+} owing to the addition of molybdate ($MoO_{2-4} + 2e + 2H_2O \rightarrow MoO_2 \cdot + 4OH^-$, $O_2 + 2H_2O + 2e \rightarrow H_2O_2 + 2OH^-$, $Ce^{3+} + H_2O_2 + 2OH^- \rightarrow Ce(OH)_4$ ($CeO_2 \cdot 2H_2O$)↓).[27,49] Fig. 6(e) displays the narrow-scan spectrum of the Mo 3d which were fitted into five peak components. The peaks located at BE of 229.25 eV, 230.41 eV and 233.71 eV are attributed to Mo $3d_{5/2}$ and Mo $3d_{3/2}$ in MoO_2,[54] while MoO_3 is identified in the Mo $3d_{5/2}$ region centered at BE of 232.32 eV and Mo $3d_{3/2}$ at 235.30 eV.[50,55] Besides, the peak at 232.32 eV may also be assigned to Mo $3d_{5/2}$ in $Al_2(MoO_4)_3$ and Na_2MoO_4,[53] which possibly co-deposited with insoluble compounds. Moreover, the content of Mo(IV) is almost equal to that of Mo(VI) according to the calculated area under relative peaks. In conclusion, the CeMCC is mainly composed of Al_2O_3, CeO_2, Ce_2O_3, MoO_2, MoO_3, $Al_2(MoO_4)_3$ and Na_2MoO_4, and cerium hydroxides.

Corrosion resistance analysis

Cupric sulfate drop test. The results of cupric sulfate drop test showed that the corrosion resistance time to $CuSO_4$-containing testing solution of the substrate was 11 s, while the anticorrosion time for CeCC and CeMCC were 62 and 95 s, respectively. It can be seen that the anticorrosion time to the

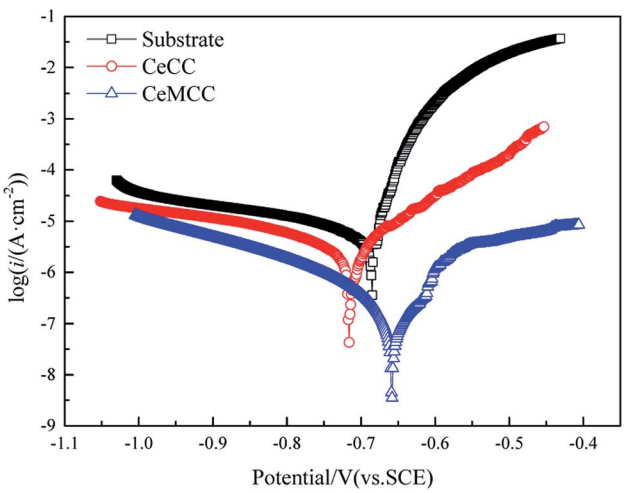

Fig. 7 Polarization curves of substrate and coated samples.

Table 2 Electrochemical parameters extracted from polarization curves

Samples	E_{corr} (V *vs.* SCE)	β_a (mV dec^{-1})	$-\beta_c$ (mV dec^{-1})	R_p (kΩ cm^2)	i_{corr} (μA cm^{-2})	Std dev. (μA cm^{-2})
Substrate	−0.69	64	297	1.7	13.36	1.27
CeCC	−0.72	102	256	7.2	4.38	0.15
CeMCC	−0.66	122	150	120.7	0.24	0.03

testing solution of the sample after Ce–Mo combined conversion treatment was significantly longer than that of the sample after Ce conversion treatment alone. Thus it can be concluded that CeMCC exhibits a good resistance to $CuSO_4^-$ containing acidic medium, in which the anticorrosion time for CeMCC could reach 95 s.

Electrochemical measurements. In the aim to examine the kinetics of inhibition process of the coated samples, the PDP experiments were performed in 3.5 wt% NaCl solution after 20 min immersion under ambient condition. Fig. 7 presents the polarization curves of bare aluminum alloy and coated samples. And the electrochemical parameters extracted from the curves, such as the corrosion potential (E_{corr}), the anodic Tafel slope (β_a) and cathodic Tafel slope ($-\beta_c$), the corrosion current density (i_{corr}) and the corresponding polarization resistance (R_p), are calculated and listed in Table 2 *via* the CHI604E software. It can be seen that the Tafel plots for the two coated samples are both at lower position in comparison with the bare sample, indicating they possess lower i_{corr} values. The E_{corr} of CeCC shifts towards more negative value (−0.72 V) compared to that of the uncoated sample (−0.69 V), which is attributed to the cathodic inhibition of coated surface.[56] While the CeMCC exhibits a slight shift towards more positive direction in E_{corr} value (−0.66 V), suggesting that the CeMCC ennobles the corrosion potential of the surface.

It is well established that i_{corr} is one of the most important parameters to evaluate the corrosion performance of material, the smaller the i_{corr} value is, the better the corrosion resistance is.[10] Reproducibility of the results was confirmed with two other spots on the sample in each case. In this study, the i_{corr} for bare sample is 13.36 μA cm^{-2}, while the i_{corr} for CeMCC is 0.24 μA cm^{-2}, about two orders of magnitude lower than the former. The i_{corr} of CeMCC is lower than that of Mohamed *et al.*,[29] but worse than that of Kanani's research,[33] in which the i_{corr} lowered from 5.1 μA cm^{-2} to 0.075 μA cm^{-2}. The strong current reduction observed for the CeMCC can be attributed to the large amount of cerium/molybdenum compounds precipitation on the substrate. Because these deposits are hydroxides or hydrated oxides with high resistance, and can also provide good barrier effect, which can insulate the substrate from the corrosive species. As a consequence, the electrochemical reactions are greatly hindered and the corrosion current density is accordingly reduced. The CeCC coated sample also shows a lower i_{corr} (4.38 μA cm^{-2}) as compared with the bare one. However, the CeCC cannot offer the same protection as the CeMCC does, which is mainly due to the fact that the aggressive ions can migrate to the metal substrate through the crevices or pores within the CeCC. The standard deviation values of i_{corr} for substrate, CeCC and CeMCC calculated by the three repeated tests were 1.27 μA cm^{-2}, 0.15 μA cm^{-2} and 0.03 μA cm^{-2}, respectively. The R_p of the CeCC is 7.2 kΩ cm^2, while the R_p of the CeMCC obtained in our alkaline Ce–Mo conversion bath is 120.7 kΩ cm^2, nearly 20 times higher than the CeCC. The R_p of CeCC is higher than the result obtained by Peter *et al.*,[31] and the R_p of CeMCC is also significantly higher that of Kanani *et al.*[33] These results demonstrate that the CeMCC possesses higher corrosion resistance than the CeCC in the corrosive electrolyte of 3.5 wt% NaCl solution.

For the sake of further investigating the anticorrosion property of the conversion coatings, EIS measurements were

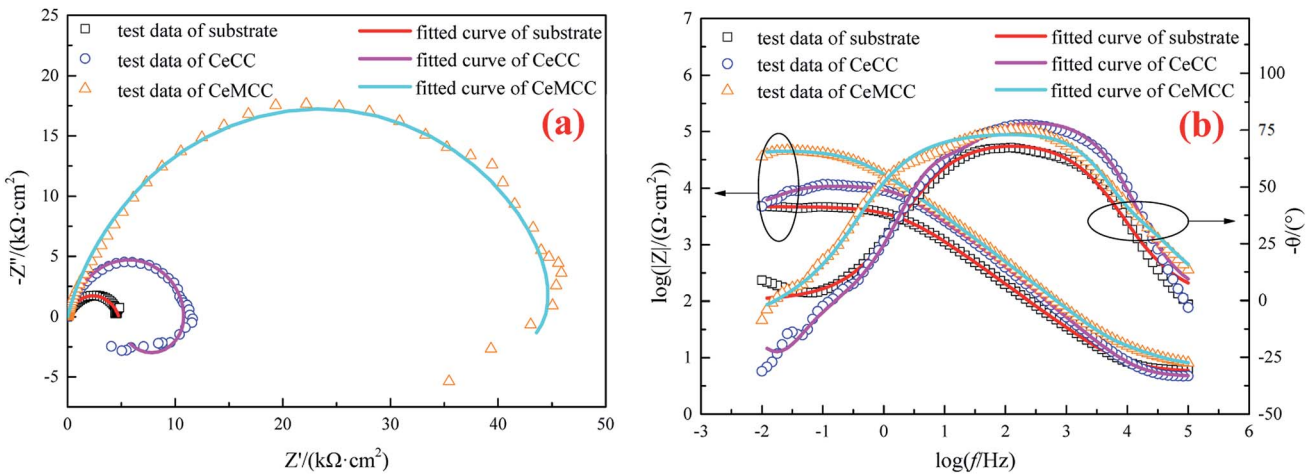

Fig. 8 EIS spectra for substrate and conversion coatings: (a) Nyquist plots and (b) Bode plots.

conducted in 3.5 wt% NaCl solution. The spectra corresponding to uncoated samples have been included for reference. As can be seen in the Nyquist plots (Fig. 8(a)), the arc for each coated sample presents a larger diameter in comparison with that of the uncoated sample, which implies a higher degree of corrosion protection. While the semicircle diameter of the CeMCC coated sample is significantly larger than that of the CeCC one, which suggests the presence of CeMCC could offer a better level of protection than CeCC. This result is in good agreement with the polarization test results above. The figure also shows an inductive behavior for both CeCC and CeMCC coated samples. The physical explanation of low-frequency inductive loop is not sufficiently clear; it has been attributed to the relaxation of adsorbed intermediate species[57] and/or formation of a passive layer and/or redox activity.[29] In this work, the inductive loop of the two coated samples may be related to redox activity, which may indicate that Ce(IV) undergoes a redox process in the low frequency region.

The Bode plots are presented in Fig. 8(b). It is well known that the impedance modulus ($|Z|$) and phase angle (θ) values extracted from Bode plots are often used to investigate the corrosion resistance of coated samples. According to the literature,[58] the $|Z|$ values imply the total resistance (solution, charge transfer and coating/oxide film resistance) and the θ values indicate the coating barrier performance. From the Bode modulus plots (the plots of $\log f$ *versus* $\log |Z|$), it can be seen that both the CeCC and the CeMCC possess higher $|Z|$ values at low frequencies compared to the bare aluminum alloy. The impedance modulus $|Z|$ value ($\log |Z|$ is nearly 4.0) of the CeCC coated sample is about three times greater than the uncoated sample, while the CeMCC coated sample presents the $|Z|$ value ($\log |Z|$ is nearly a constant about 4.7) more than one order of magnitude higher than the bare one. The increase in $|Z|$ value in the case of CeCC coated sample may be thanks to the active inhibition role of Ce(III)/Ce(IV) species in the coating which could heal the corroded areas and thus inhibit the corrosion reactions.[28] Different from CeCC, the increment of $|Z|$ value for CeMCC may be attributed to the insoluble molybdenum oxides precipitation on the metal surface. These compounds act as a barrier layer to impede the access of Cl^- to the substrate and reduce the number of anodic sites on the alloy surface. As a result, the rate of electron generation can be reduced, leading to the decrease of corrosion rate. In the Bode phase plots (the curves of $\log f$ *versus* $-\theta$), the first relaxation process at the frequency region ranged from 1000 to 1 Hz of the two conversion coatings has a θ value very close to 80°, indicating the electrochemical process on the surface shows a capacitive behavior with good dielectric properties.[59] In other words, the interface of solution/conversion coatings has the ability to charge and hence avoid the ionic flow of corrosive medium.[59] What is more, the CeMCC coated sample exhibits a greater flattening of the maximum in the diagram. This is a further indication that these compounds could provide a better protection level owing to their barrier effect. In contrast, the substrate shows a θ value slightly higher than 65°, since its capacitive properties are poorer than those of the two conversion coatings. In addition, with the decrease of the frequency, the phase angle tends to drop and results in a second relaxation process, related to the permeation of the electrolyte through the pores or cracks reaching the underlying metal surface.[60]

The EIS data for the substrate and the coated samples were fitted using equivalent circuits (ECs) illustrated in Fig. 9, where R_s represents the resistance of the electrolyte between the reference electrode and the sample surface. For the bare 6063, the EC (Fig. 9(a)) is formed by R_s series with a constant phase element (CPE) in parallel with a second resistance (R_c) representing the aluminum oxide film properties. The impedance of the CPE is defined as:[61]

$$Z_{CPE} = Q/(j\omega)^n$$

where Q is a constant, j is an imaginary coefficient, ω is angular frequency and n (defined from 0 to 1) is related to surface homogeneity.

While in the EC for coated samples (see in Fig. 9(b)), the R_c accounts for the resistance of cracks or pores when immersion in NaCl solution, and in series with a circuit consisting of C_{dl}, R_{ct} and R_L series with L in parallel, representing the double layer capacitance on the interface of coating/substrate, the charge transfer resistance associated with corrosion process, the inductance resistance, and the inductance element, respectively. Since a conversion coating is generally not simplified as a pure capacitance, the two conversion coatings were simulated as CPE components in the electrochemical model. It is noteworthy that these models were choice due to displayed highest goodness to fit experimental data of the as-prepared samples.

The EIS spectra of the samples were fitted according to the ECs in Fig. 9, and the fitted results are in good agreement with the experimental data (see Fig. 8(a) and (b)). The chi-squared (χ^2) error value was of the order of 10^{-3} for all cases,

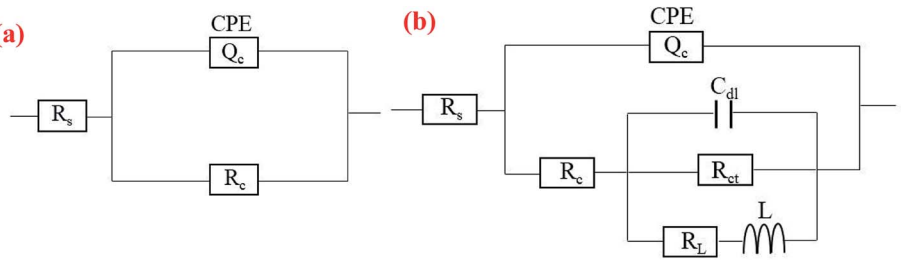

Fig. 9 Equivalent circuits used to fit the impedance data for (a) bare AA6063 and (b) coated samples.

Table 3 EIS simulated parameters for bare AA6063 and coated samples by using the ECs in Fig. 9

		CPE						
Samples	R_s (Ω cm^2)	Y (μS $s^n \cdot$cm^{-2})	n	R_c (Ω cm^2)	C_{dl} (μF cm^{-2})	R_{ct} (kΩ cm^2)	R_L (kΩ cm^2)	L (kH cm^{-2})
Substrate	5.6	29.7	0.79	4751	—	—	—	—
CeCC	4.6	7.1	0.90	4820	4.5	6.1	5.6	35.8
CeMCC	6.9	10.2	0.79	38.1	0.5	47.1	229.2	4610

indicating that the ECs used to model sample/NaCl solution system were appropriate. The simulated parameters extracted from the models are given in Table 3. The table shows that the R_s values are between 4 and 7 Ω cm^2, indicating high conductivity of the 3.5 wt% NaCl solution. The lower values of Y for CeCC and CeMCC may confirm the excellent insulating property of the coatings, which results in high resistance for electrochemical reactions taking place on the surface. And the C_{dl} for CeMCC is 0.5 μF cm^{-2}, nearly 10 times lower than the CeCC one, indicating that the number of cracks or pores developed on the CeMCC is less than those on CeCC surface. The value of R_{ct} for CeMCC is almost 8 times higher than the CeCC one, corroborating the enhanced barrier property of the conversion coating and the fact that the compact layer of CeMCC offers better corrosion resistance than the CeCC does. In addition, the R_L and L values of CeMCC are about 40 times and 130 times respectively higher than that of CeCC. The results above correspond well to the PDP results.

Mechanism of inhibition. The results of electrochemical techniques demonstrate superior corrosion-inhibiting properties of cerium-based conversion treatment with the addition of molybdate. The inhibiting effect can be described by considerable decrease of i_{corr}, as was observed in the polarization measurements (Fig. 7), and increased impedance ($|Z|$, R_{ct} and R_L) observed by EIS measurements (Fig. 8 and Table 3). The inhibiting mechanism of cerium species has been discussed in many researches and is associated with the formation of highly insoluble oxides/hydroxides of cerium preferentially in active cathodic sites.[62–64]

According to the literature,[62,64,65] the inhibition mechanism of cerium treatment consists of two steps: (1) insoluble oxides/hydroxides of cerium are formed owing to interaction with hydroxyl ions on the cathodic sites and (2) the formed insoluble cerium compounds precipitate on the intermetallics, creating a barrier to the supply of oxygen or electrons to the oxygen reduction reaction. Thus the cathodic reaction is inhibited and the corresponding anodic reaction significantly reduces. And Yasakau *et al.* also reported that the inhibiting mechanism of cerium molybdate nanowires is related to the formation of thin protective layer on the top of intermetallics and surrounding alloy matrix.[27,66]

While in the present study, the mechanism of inhibition of CeMCC is most probably related to the synergistic inhibiting action of cerium and molybdate ions present in the conversion solution. The formation of cerium oxides/hydroxides deposits is expected to occur near cathodic areas, while molybdenum oxides/hydroxides may precipitate on the entire alloy surface. Considering the criteria for corrosion inhibitors to be used in active protective treatments: soluble in water combined with fast, effective and irreversible inhibition,[67] the inhibitive activity of CeMCC treatment makes it functionally attractive for inclusion in active protective treatments.

Influenced by the inertia thinking that the metallic materials could only be dissolved in acid solution, nearly all researches on chrome-free conversion treatment have been concentrated in acid range for several decades. However, for aluminum alloys, researchers in the field may have overlooked the fact that aluminum can also be dissolved in alkaline solutions. In this study, a Ce–Mo based conversion coating was prepared with an alkaline conversion bath, and the studies on the coating indicated that the conversion treatment was a cathodic protection treatment according to the results of EDS, PDP, EIS and β_c. And compared with the poor stability of acidic bath, the stability of our alkaline conversion bath can be maintained for at least three months. However, there are some problems that need to be further studied. The treatment time is too long, the treatment temperature is too high, and the coating formation mechanism under alkaline condition is still unknown. The results of these studies will be reported in our next article.

Conclusion

Cerium-based conversion treatment (without and with molybdate) by alkaline methods was investigated on aluminum alloy 6063. The CeMCC possesses a smoother and more uniform morphology compared to the CeCC. The thickness of CeCC and CeMCC are about 0.8 and 1.2 μm respectively. The XPS depth analysis indicates that CeMCC possesses considerable amount of molybdenum and its cerium content is higher than that of CeCC at all coating depths. CeCC is comprised of Al_2O_3, Ce_2O_3, CeO_2, and cerium hydroxides; and CeMCC is made up of Al_2O_3, CeO_2, Ce_2O_3, MoO_2, MoO_3, $Al_2(MoO_4)_3$, Na_2MoO_4 and cerium hydroxides. The anticorrosion time of cupric sulfate drop test for CeCC and CeMCC are 62 and 95 s, respectively. The CeMCC exhibits better corrosion protection, with a lower i_{corr} of 0.24 μA cm^{-2} compared to 4.38 μA cm^{-2} for the CeCC in 3.5 wt% NaCl solution. And the CeMCC also presents a higher R_p value (120.7 kΩ cm^2), nearly 20 times higher than the CeCC. In the EIS analysis, the R_{ct} of 47.1 kΩ cm^2, C_{dl} of 0.5 μF cm^{-2}, R_L of 229.2 kΩ cm^2 and L of 4610 kH cm^{-2} for CeMCC well explained the reason why CeMCC presents better barrier property than the CeCC one.

Conflicts of interest

There are no conflicts to declare.

Acknowledgements

This work was supported by Science and Technology Program of Guangzhou, China (grant no. 201804010348) and by the Guangdong Basic and Applied Basic Research Foundation (grant no. 2020A1515010006).

References

1 M. Witkowska, G. E. Thompson, T. Hashimoto and E. Koroleva, *Surf. Interface Anal.*, 2013, **45**, 1585–1589.
2 L. Xu, R. Guo, C. Tang and J. ZHANG, *Surf. Technol.*, 2011, **40**, 78–80.
3 J. C. Williams and E. A. Starke Jr, *Acta Mater.*, 2003, **51**, 5775–5799.
4 Z. Feng, G. S. Frankel and C. A. Matzdorf, *J. Electrochem. Soc.*, 2014, **161**, C42–C49.
5 O. Lunder, F. Lapique, B. Johnsen and K. Nisancioglu, *Int. J. Adhes. Adhes.*, 2004, **24**, 107–117.
6 R. Grilli, M. A. Baker, J. E. Castle, B. Dunn and J. F. Watts, *Corros. Sci.*, 2011, **53**, 1214–1223.
7 C. Liang, Z. Lv, Y. Zhu, S. Xu and H. Wang, *Appl. Surf. Sci.*, 2014, **288**, 497–502.
8 R. Uma Rani, A. K. Sharma, S. M. Mayanna, H. Bhojraj and D. R. Bhandari, *Surf. Eng.*, 2005, **21**, 198–203.
9 B. Ramezanzadeh, H. Vakili and R. Amini, *Appl. Surf. Sci.*, 2015, **327**, 174–181.
10 A. Yi, W. Li, J. Du and S. Mu, *Appl. Surf. Sci.*, 2012, **258**, 5960–5964.
11 L. Lei, J. Shi, X. Wang, D. Liu and H. Xu, *Appl. Surf. Sci.*, 2016, **376**, 161–171.
12 A. K. Mishra and R. Balasubramaniam, *Corros. Sci.*, 2007, **49**, 1027–1044.
13 J. Hu, X. H. Zhao, S. W. Tang, W. C. Ren and Z. Y. Zhang, *Appl. Surf. Sci.*, 2007, **253**, 8879–8884.
14 M. Dabala, K. Brunelli, E. Napolitani and M. Magrini, *Surf. Coat. Technol.*, 2003, **172**, 227–232.
15 M. Bethencourt, F. J. Botana, J. J. Calvino, M. Marcos and M. A. Rodriguez-Chacon, *Corros. Sci.*, 1998, **40**, 1803–1819.
16 A. De Nicolò, L. Paussa, A. Gobessi, A. Lanzutti, C. Cepek, F. Andreatta and L. Fedrizzi, *Surf. Coat. Technol.*, 2016, **287**, 33–43.
17 A. Uhart, J. B. Ledeuil, D. Gonbeau, J. Dupin, J. Bonino, F. Ansart and J. Esteban, *Appl. Surf. Sci.*, 2016, **390**, 751–759.
18 B. Hinton and L. Wilson, *Corros. Sci.*, 1989, **29**, 967–985.
19 A. P. Loperena, I. L. Lehr and S. B. Saidman, *J. Magnesium Alloys*, 2016, **4**, 278–285.
20 C. Wang, F. Jiang and F. Wang, *Corros. Sci.*, 2004, **46**, 75–89.
21 C. Wang, G. Wu, Q. Zhang and L. Jiang, *J. Mater. Sci.*, 2008, **43**, 3327–3332.
22 W. Chunyu, Z. Qiang, Z. Ji and W. Gaohui, *J. Rare Earths*, 2006, **24**, 64–67.
23 F. Mansfeld, S. Lin, S. Kim and H. Shih, *Electrochim. Acta*, 1989, **34**, 1123–1132.
24 M. A. Arenas, M. Bethencourt, F. J. Botana, J. De Damborenea and M. Marcos, *Corros. Sci.*, 2001, **43**, 157–170.
25 D. R. Arnott, B. Hinton and N. E. Ryan, *Corrosion*, 1989, **45**, 12–18.
26 K. A. Yasakau, S. Kallip, M. L. Zheludkevich and M. G. S. Ferreira, *Electrochim. Acta*, 2013, **112**, 236–246.
27 K. A. Yasakau, J. Tedim, M. L. Zheludkevich, R. Drumm, M. Shem, M. Wittmar, M. Veith and M. G. S. Ferreira, *Corros. Sci.*, 2012, **58**, 41–51.
28 Z. Mahidashti and B. Ramezanzadeh, *J. Rare Earths*, 2018, **36**, 1112–1120.
29 M. Gobara, A. Baraka, R. Akidb and M. Zorainy, *RSC Adv.*, 2020, **10**, 2227–2240.
30 P. Rodič, I. Milošev, M. Lekka, F. Andreatta and L. Fedrizzi, *Electrochim. Acta*, 2019, **308**, 337–349.
31 P. Rodič and I. Milošev, *Corros. Sci.*, 2019, **149**, 108–122.
32 M. Eslami, M. Fedel, G. Speranza, F. Deflorian and C. Zanella, *J. Electrochem. Soc.*, 2017, **164**, C581–C590.
33 M. Kanani, I. Danaee and M. H. Maddahy, *Mater. Corros.*, 2014, **65**, 1073–1079.
34 H. Hassannejad, M. Moghaddasi, E. Saebnoori and A. R. Baboukani, *J. Alloys Compd.*, 2017, **725**, 968–975.
35 P. Campestrini, H. Terryn, A. Hovestad and J. De Wit, *Surf. Coat. Technol.*, 2004, **176**, 365–381.
36 M. Dabalà, L. Armelao, A. Buchberger and I. Calliari, *Appl. Surf. Sci.*, 2001, **172**, 312–322.
37 J. Zhang, W. Li, J. Du, D. Han and X. Zheng, *Chin. Sci. Bull.*, 2010, **55**, 3345–3349.
38 M. Eslami, M. Fedel, G. Speranza, F. Deflorian, N. Andersson and C. Zanella, *Electrochim. Acta*, 2017, **255**, 449–462.
39 S. A. Kulinich, A. S. Akhtar, P. C. Wong, K. C. Wong and K. A. R. Mitchell, *Thin Solid Films*, 2007, **515**, 8386–8392.
40 T. Lostak, A. Maljusch, B. Klink, S. Krebs, M. Kimpel, J. Flock, S. Schulz and W. Schuhmann, *Electrochim. Acta*, 2014, **137**, 65–74.
41 F. Andreatta, A. Turco, I. De Graeve, H. Terryn, J. De Wit and L. Fedrizzi, *Surf. Coat. Technol.*, 2007, **201**, 7668–7685.
42 O. Lunder, F. Lapique, B. Johnsen and K. Nisancioglu, *Int. J. Adhes. Adhes.*, 2004, **24**, 107–117.
43 D. Chidambaram, C. R. Clayton and G. P. Halada, *Electrochim. Acta*, 2006, **51**, 2862–2871.
44 X. Yu and G. Li, *J. Alloys Compd.*, 2004, **364**, 193–198.
45 J. A. DeRose, T. Suter, A. Bałkowiec, J. Michalski, K. J. Kurzydlowski and P. Schmutz, *Corros. Sci.*, 2012, **55**, 313–325.
46 H. Ardelean, I. Frateur and P. Marcus, *Corros. Sci.*, 2008, **50**, 1907–1918.
47 M. Romeo, K. Bak, J. El Fallah, F. Le Normand and L. Hilaire, *Surf. Interface Anal.*, 1993, **20**, 508–512.
48 R. C. Furneaux, G. E. Thompson and G. C. Wood, *Corros. Sci.*, 1978, **18**, 853–881.
49 K. A. Yasakau, M. L. Zheludkevich, S. V. Lamaka and M. G. Ferreira, *J. Phys. Chem. B*, 2006, **110**, 5515–5528.
50 C. D. Wanger, W. M. Riggs, L. E. Davis, J. F. Moulder and G. E. Muilenberg, *Handbook of X-ray photoelectron*

spectroscopy, Perkin-Elmer Corporation, Eden Prairie, Minnesota, 1979.
51 B. Brox and I. Olefjord, *Surf. Interface Anal.*, 1988, **13**, 3–6.
52 D. S. Zingg, L. E. Makovsky, R. E. Tischer, F. R. Brown and D. M. Hercules, *J. Phys. Chem.*, 1980, **84**, 2898–2906.
53 T. A. Patterson, J. C. Carver, D. E. Leyden and D. M. Hercules, *J. Phys. Chem.*, 1976, **80**, 1700–1708.
54 T. Schroeder, J. Zegenhagen, N. Magg, B. Immaraporn and H. Freund, *Surf. Sci.*, 2004, **552**, 85–97.
55 J. Choi and L. T. Thompson, *Appl. Surf. Sci.*, 1996, **93**, 143–149.
56 G. Yoganandan, K. Pradeep Premkumar and J. N. Balaraju, *Surf. Coat. Technol.*, 2015, **270**, 249–258.
57 U. Donatus, J. V. de Sousa Araujo, C. de Souza Carvalho Machado, N. V. V. Mogili, R. A. Antunes and I. Costa, *Corros. Eng., Sci. Technol.*, 2019, **54**, 205–215.
58 B. Ramezanzadeh and M. Rostami, *Appl. Surf. Sci.*, 2017, **392**, 1004–1016.
59 E. Onofre-Bustamante, M. A. Dominguez-Crespo, A. M. Torres-Huerta, A. Olvera-Martínez, J. Genescá-Llongueras and F. J. Rodríguez-Gómez, *J. Solid State Electrochem.*, 2009, **13**, 1785–1799.
60 E. Cano, D. M. Bastidas, V. Argyropoulos, S. Fajardo, A. Siatou, J. M. Bastidas and C. Degrigny, *J. Solid State Electrochem.*, 2010, **14**, 453–463.
61 G. J. Brug, A. L. G. van den Eeden, M. Sluyters-Rehbach and J. H. Sluyters, *J. Solid State Electrochem.*, 1984, **176**, 275–295.
62 K. A. Yasakau, M. L. Zheludkevich, S. V. Lamaka and M. G. S. Ferreira, *J. Phys. Chem. B*, 2006, **110**, 5515–5528.
63 A. E. Hughes, J. D. Gorman, P. R. Miller, B. A. Sexton, P. J. K. Paterson and R. J. Taylor, *Surf. Interface Anal.*, 2004, **36**, 290–303.
64 B. R. W. Hinton, *J. Alloys Compd.*, 1992, **180**, 15–25.
65 M. A. Jakab, F. Presuel-Moreno and J. R. Scully, *J. Electrochem. Soc.*, 2006, **153**, B244–B252.
66 K. A. Yasakau, J. Tedim, M. F. Montemor, A. N. Salak, M. L. Zheludkevich and M. G. S. Ferreira, *J. Phys. Chem. C*, 2013, **117**, 5811–5823.
67 M. W. Kendig and R. G. Buchheit, *Corrosion*, 2003, **59**, 379–400.

